Coherent Multidimensional Vibrational Spectroscopy of Representative N-Alkanes

Nathan A. Mathew, Mark A. Rickard, Kathryn M. Kornau, Andrei V. Pakoulev, Stephen B. Block, Lena A. Yurs, and John C. Wright*

Department of Chemistry, University of Wisconsin, Madison, Wisconsin 53706

Received: June 2, 2009; Revised Manuscript Received: July 21, 2009

Mixed frequency/time domain, two color triply vibrationally enhanced (TRIVE) four wave mixing (FWM) spectroscopy is used to study the methyl and methylene modes in octane and dotriacontane. The experiments involve scanning different combinations of the two excitation frequencies, the monochromator frequency, and the two time delays between the three excitation pulses while the remaining variables are fixed. Two dimensional spectra of the methyl and methylene stretching region have weak, asymmetrical diagonal- and cross-peaks when the excitation pulses are temporally overlapped. As the time delays change, the spectra change as new peaks appear and their peak intensity and position change. Combined two-dimensional scans of the excitation frequency and time delay show the changes are caused by relaxation of the initially excited populations to other states that are coupled to the methyl and methylene stretching modes. Two dimensional time delay scans show that the coherence dephasing rates are very fast so fully coherent TRIVE FWM pathways involving multiple quantum coherences are not possible without shorter excitation pulses. Similar experiments involving the methyl and methylene bend and stretching modes identify cross-peaks between these modes and population transfer processes that create cross-peaks. The asymmetric methylene stretch/Fermi resonance band is observed to contain unresolved states that couple differently with the symmetric methylene stretching and scissor modes as well as with lower lying quantum states that are fed by population transfer. The TRIVE FWM data show that the multidimensional spectra are dominated by rapid population transfer within the methyl and methylene stretching modes and to lower quantum states that are coupled to the stretching modes.

1.0. Introduction

Vibrational spectroscopy is used extensively for chemical measurement because it is sensitive to molecular structure. Spectral congestion, line broadening, and solvent contributions frequently limit its applicability in complex samples. Recently, a new family of coherent multidimensional vibrational spectroscopies (CMDVS) has been developed that is an optical analogue of multidimensional nuclear magnetic resonance (NMR).[1−4] It promises to increase the spectral selectivity for complex samples in the same way as multidimensional NMR increased selectivity in biological samples.[5] These methods are based upon four wave mixing where three coherent excitation beams excite multiple quantum states within the dephasing times of their coherences.[6] The three transitions create a coherent time-dependent superposition state. Each pair of states in the superposition state reradiates light at the frequency differences between each pair. Since the excitation beams are spatially and temporally coherent, the ensemble of pairs are also coherent, so their emission occurs as beams whose directions are defined by momentum conservation. CMDVS methods divide into those based on time domain measurements where the light's temporal phase oscillations are measured by incrementing the time delays between the excitation pulses and frequency domain measurements where the output intensity enhancements are measured as a function of the excitation frequencies.[6]

Time domain methods require long-term phase stability during the measurement time. These methods are collectively called time domain 2D-IR, and they include stimulated photon echo, transient grating, reverse photon echo, and reverse transient grating methods.[2] Here, the excitation pulses are short compared with the dephasing time. Multidimensional spectral features require anharmonic coupling that shifts the frequency of combination bands and overtone transitions so that destructive interference does not eliminate the net contributions from different coherence pathways. The output beams result from free induction decay (FID) that occurs during the time that the quantum mechanical superposition state remains coherent and driven emission that occurs during the excitation pulses.

Frequency domain CMDVS methods require short-term phase stability during the quantum states dephasing times. The excitation pulses are long compared with the dephasing time. They include singly vibrationally enhanced (SIVE),[7−10] doubly vibrationally enhanced (DOVE),[4,11−16] and triply vibrationally enhanced (TRIVE) four wave mixing (FWM).[1,17−19] Multidimensional features in TRIVE experiments require the same anharmonic couplings as time domain 2D-IR. Multidimensional features in DOVE experiments require anharmonic couplings that create combination band and overtone transitions. The output beams result from a nonlinear polarization that is driven by the electric fields of the excitation pulses. If the excitation pulse widths are comparable to the coherence dephasing times, then these methods become mixed frequency/time domain methods and can measure both spectral and temporal dependences.[1] The pulses are temporally long enough that their frequency bandwidth resolves spectral features as one scans the excitation frequencies but are short enough that they resolve the dynamics as one scans the time delays between excitation pulses.

The output beam is super-radiant because the phased array of emitting states cooperatively creates a coherent beam whose intensity increases quadratically with the concentration of emitting states. Although this beam is much brighter than

---

* Corresponding author.

10.1021/jp905172p CCC: $40.75

equivalent incoherent emission, the inefficiency of infrared detectors has limited most time domain 2D-IR and TRIVE FWM studies. The FWM intensity depends on the square of the product of four transition moments, so weak transitions make it increasingly difficult to observe signal. Typically, time domain 2D-IR methods use heterodyne detection to improve the detection efficiency. Even with heterodyne detection, 2D-IR has traditionally been restricted to the strongest infrared transitions such as carbonyl, amine, and hydroxyl stretching modes. This limitation is different for CMDS methods such as DOVE-FWM that create a visible or UV output at a different frequency than the excitation beams. Consequently, they are sensitive to much weaker infrared transitions.

It is important to extend the CMDS methods to include the weaker infrared transitions that are more typical of vibrational spectroscopy. Recent work has used relaxation-assisted two-color 2D-IR to observe a wide variety of different vibrational transitions.[20−22] Here, two excitations create a population in a strongly allowed vibrational mode. Vibrational relaxation from this initial mode populates other modes and propagates the original vibrational energy to other parts of a molecule. If these other modes are anharmonically coupled to a second mode, then a third excitation pulse can excite the second mode and create a cross-peak at the frequencies of the first and last transitions. Relaxation assisted 2D-IR enhances the intensity of cross-peaks by factors >20 compared with the value for direct coupling of the two modes.

The C−H vibrational modes are important features in the infrared and Raman spectra of organic molecules, and it is expected that they will play an important role in the emerging techniques of coherent multidimensional vibrational spectroscopy (CMDVS). A great deal of work has been done to understand vibrational relaxation in the simplest molecules containing isolated $-CH_3$ and $-CH$ groups.[23−39] Iwaki and Dlott's work on methanol[40,41] and early work on ethanol[38,39] are the most relevant to the work reported in this paper on larger alkanes. Iwaki and Dlott find that excitation of a methyl stretching mode in methanol relaxes in three stages. The methyl stretching modes first equilibrate and relax to the CH and OH bending modes (1−2 ps). These modes then relax to the methyl rocking and CO stretching modes (2−5 ps). Finally, these modes relax to bath modes (5−15 ps). Estimates of the methyl asymmetric and symmetric state lifetimes are 5 and 1 ps, respectively, and the rate constant for transfer from the symmetric to asymmetric stretch mode is 6×10^{11} s^{-1}. In ethanol, the lifetimes of the vibrational states are longer, presumably because of larger energy mismatches between the C−H stretching modes and bending overtones. Excitation of a C−H stretching mode results in redistribution among all of the C−H stretching modes in <0.5 ps. The lifetime of the methyl asymmetric stretch mode is 12 ps.

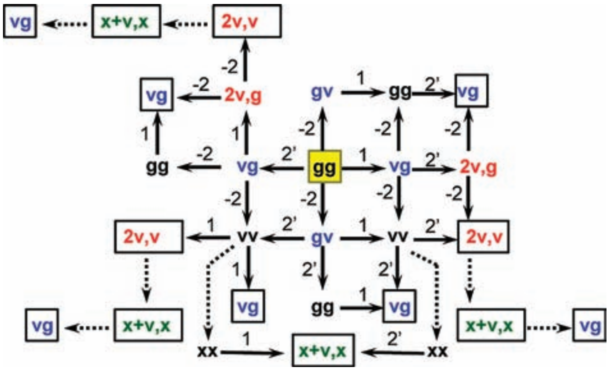

Figure 1. Liouville diagram showing the evolution of the coherences (colored) and populations resulting from the initial ground state population given by *gg* evolving from all time orderings of interactions with excitation frequencies ω_1, ω_2, $\omega_{2'}$ and the phase-matching $\vec{k}_4 = \vec{k}_1 - \vec{k}_2 + \vec{k}_{2'}$. The diagram assumes all three frequencies are identical. Solid arrows represent interactions with the excitation fields and dotted arrows represent population transfer. The boxes indicate the initial population (highlighted in yellow) and the final output coherences. Coherences involving only fundamental modes are blue; overtone and combination bands are red, and combination bands with unknown states are green.

In this paper, we report the results of mixed frequency/time domain TRIVE FWM experiments on the methyl and methylene stretching and bending modes. The 2D spectra taken with temporally overlapped excitation pulses exhibit weak cross-peaks which become increasingly important when the first two pulses create a vibrational population and the third pulse is delayed. At longer delay times, new cross-peaks appear and many times acquire a doublet structure. The dependence of the spectral features on the time delays show that the methylene and methyl coherences have dephasing times that are much faster than the excitation pulse widths, so only the FWM pathways with intermediate populations contribute significantly. In addition, the populations relax quickly to other states, so new FWM pathways become important. These states then create the FWM pathways responsible for the increased intensity of the weak cross-peaks and the development of the new spectral features. Changing the excitation delay times allows direct observation of the population relaxation dynamics both between the different C−H modes and between the C−H modes and the lower energy vibrational modes that couple to the C−H modes. A second consequence of the different pathways is the presence of cross-peaks with the band containing the unresolved methylene asymmetric stretch and Fermi resonance states. The cross-peaks' frequencies are not centered on the band but are shifted to different positions within the band. The cross-peak positions reflect the different couplings with unresolved states compromising the band.

2.0. Theoretical Section

The TRIVE FWM experiments use two excitation sources with frequencies ω_1 and ω_2. A beam splitter divides the latter into two beams labeled 2 and 2′, and the beams are crossed in the sample at angles that meet the phase-matching condition $\vec{k}_4 = \vec{k}_1 - \vec{k}_2 + \vec{k}_{2'}$. A monochromator spectrally isolates the output frequency. Note that subscripts designate the frequencies, not the time ordering. Twelve coherence pathways can create cross-peaks, and 16 pathways can create diagonal-peaks for this phase-matching geometry.[17,18] If population transfer occurs, there are additional pathways with new output coherences for both cross-peaks and diagonal-peaks.[20−22] The Liouville diagrams for the diagonal-peak and cross-peak pathways appear in Figure 1 and Figure 2, respectively. These diagrams are particularly useful because they show the relationships between all of the coherence pathways that are important for this work. They show the temporal evolution of the coherences (indicated by colored letters) and populations (indicated by black letters). The letters designate the ket and bra states of the $|i\rangle\langle j|$ coherence (or population) where *i* and *j* are the ket and bra states, respectively. The arrows indicate interactions that change states; the numbers above the arrows designate the ω_1 and ω_2 excitation frequencies; the dotted arrows indicate population transfer, and the boxes designate the initial ground state population (i.e., *gg*) and the final output coherences (e.g., $v'g$; vg; $2v,v$; $v + v',v$; $v + x,x$;

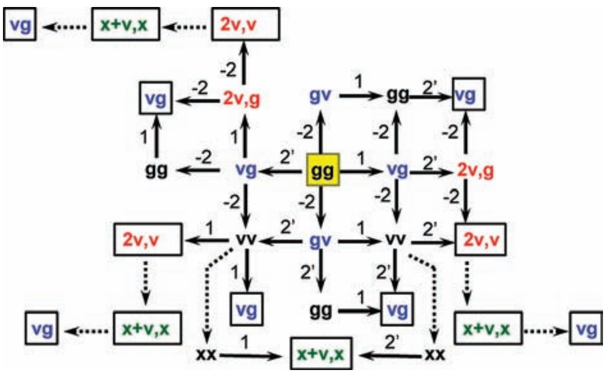

Figure 2. Similar Liouville diagram to Figure 1 but showing the evolution of the coherences and populations when ω_1 is different from ω_2, $\omega_{2'}$.

$v' + x,x$). The ground state population is highlighted in yellow since it is the starting point for all pathways. The state labels $2v$, $v + v'$, and x designate overtone, combination band, and unknown states that may be populated by relaxation from the higher energy states. Coherences involving overtone and combination band states are colored red while those involving only fundamental modes are colored blue. Combination band states involving unknown states are colored green. The v and v' label known CH vibrational modes. Our diagrams assume that ω_2 is resonant with a transition involving v and ω_1 is resonant with v' for cross-peaks and v for diagonal peaks.

First, consider the pathways without population transfer in Figure 1 and Figure 2. The cross-peak pathways create output coherences such as $v'g$ and $(v + v',v)$ while the diagonal-peak pathways create output coherences such as vg and $(2v,v)$. The frequencies of the combination band and overtone output coherences are anharmonically shifted from those involving the fundamental modes. When the ω_1 and ω_2 excitation frequencies are resonant with the two different vibrational modes of a cross-peak, eight pathways are fully coherent and involve zero quantum intermediate coherences (labeled $v'v$) or double quantum coherences (labeled $v + v',g$) and four involve intermediate populations (labeled gg or vv). An additional four coherence pathways describe diagonal-peaks where ω_1 and ω_2 excite the same vibrational mode. When a pathway involves an overtone or combination band transition, there are eight coherence pathways that define the output.[1,17−19,42]

The pathways that involve population transfer have been described by Rubtsov as relaxation assisted pathways.[20−22] In population transfer, an excited state population relaxes from state v' to state v. Population transfer causes new cross-peaks due to two mechanisms. The first is direct population transfer where interaction with ω_2 and $\omega_{2'}$ creates a v' state population which subsequently relaxes to state v over the delay time between the ω_2 and the ω_1 beams, $\tau_{21} \equiv \tau_2 - \tau_1$. Subsequent interaction with ω_1 causes transitions from state v resulting in a four wave mixing enhancement. The maximum intensity occurs when the delay time is long enough to transfer significant population but short enough that the v state population has not relaxed. The second is the indirect mechanism observed by Rubtsov and co-workers[20−22] where a population relaxes to state x which is anharmonically coupled to state v. Subsequent excitation of state v results in a four wave mixing signal and a cross-peak if the coupling from the population in state x shifts the frequency of $x \leftrightarrow x + v$ transitions or changes their dynamics. State x can be any state that is anharmonically coupled to state v. It is not under the control of the experimenter. This second mechanism usually results in peak position shifts. In Figure 1 and Figure 2, this mechanism corresponds to pathways involving the "x" states. Rubtsov was able to determine the presence of these x states though anharmonic shifts created when these populated x states interacted with the final coherence. In our work, x state examples could be C−H bending modes or carbon backbone motions.

As an example, consider the two pathways $gg \xrightarrow{-2} gv \xrightarrow{2'} gg \xrightarrow{1} v'g$ and $gg \xrightarrow{-2} gv \xrightarrow{2'} vv \xrightarrow{1} v + v',v$ where $v + v'$ designates a combination band state. The $v'g$ and $v + v',v$ output coherences are out-of-phase and their radiated fields will cancel if they have identical frequencies and dynamics. If the v and v' states are anharmonically coupled, the frequencies and/or dynamics will differ, the interference will be incomplete, and both coherences contribute to the cross-peaks. Typically, one sees two peaks that are separated by the anharmonic shift. If population transfer occurs, then the second pathway changes to one of two possibilities. A direct process occurs when the population transfer occurs to a state that is excited by successive excitation pulses. An example pathway is $gg \xrightarrow{-2} gv \xrightarrow{2'} vv \Rightarrow v'v' \xrightarrow{1} v'g$ where the double arrow indicates population transfer. An example of an indirect pathway is $gg \xrightarrow{-2} gv \xrightarrow{2'} vv \Rightarrow xx \xrightarrow{1} x + v',x$. The cross-peaks still appear if the x and v' states are coupled, but the shift in the two coherences' frequency will be different because the anharmonic shift is different. Note that there is no spectral information about the identity of the x state other than the anharmonic shift.

Figure 1 and Figure 2 also contain pathways such as $gg \xrightarrow{-2} gv \xrightarrow{2'} vv \xrightarrow{1} v + v',v \Rightarrow x + v',x$. This pathway is closely related to population transfer pathways, but the transfer occurs between coherences rather than populations. The anharmonic coupling in the states forming the two coherences is different, so the coherence frequency changes in the transfer. Since vv populations do not oscillate, the transfer is not the same as a population transfer, but it still creates pathways that must be considered for a full treatment of the system dynamics.

If the pathways are restricted to transitions that involve only fundamentals, and if we assume the excitation pulse durations are longer than the dephasing times, the dependence of the output coherence on the excitation frequencies can be approximated assuming the steady state approximation and the dominance of fully resonant processes.[6,43] With these assumptions, the output nonlinear polarization for a cross-peak involving only the v and v' fundamental modes and no population transfer is

$$P = \mu_{v'g} N \rho_{v'g} = -\frac{N\mu_{vg}^{2}\mu_{v'g}^{2} E_1 E_2 E_{2'}}{8\hbar^3 \Delta_{v'g}\Delta_{vg}^{*}} \times \left(\frac{1}{\Delta_{v'g}} + \frac{2\Gamma_{vg}}{\Gamma_{gg}\Delta_{vg}} + \frac{i\Gamma_{v'v}^{g}}{\Delta_{v'v}\Delta_{v'g}}\right) \qquad (1)$$

where $\Delta_{ba} = \delta_{ba} - i\Gamma_{ba}$; δ_{ba}, and Γ_{ba} are the detuning from resonance and dephasing rate of the ba coherence; μ_{ba} is the transition moment for the $b \leftrightarrow a$ transition; N is the molecular number density; E_i is the electric field at ω_i, and $\Gamma_{ba}^{g} \equiv \Gamma_{ba}^{*} - \Gamma_{bg}^{*} - \Gamma_{ag}^{*} - \Gamma_{gg}$ where Γ_{ba}^{*} is the pure dephasing rate. Since $\Gamma_{bg} > \Gamma_{gg}$, the second term in equation will dominate over the first term. The last term vanishes if there is no pure dephasing and can be considered a dephasing induced resonance.[44] Since pure dephasing is likely to be important for the n-alkane C−H modes, the last term will contribute. Note that it contains the zero quantum coherence resonance involving v and v'.

The output intensity depends quadratically on the polarization and therefore has a $\mu_{vg}^4\mu_{v'g}^4$ dependence on the transition moments. The IR absorption coefficients for the C−H modes are at least an order of magnitude weaker than those of the strong C=O stretch modes that are commonly used in 2D-IR experiments. Since the absorption coefficients scale as μ^2, the output intensity is at least 4 orders of magnitude lower than experiments using modes with large absorption coefficients. Although this intensity difference seems large, FWM methods have large dynamic ranges and strong signals because the emission is coherent and directional. For example, doubly vibrationally enhanced (DOVE) FWM produces large signals with combination bands that have an order of magnitude lower absorption coefficient than the C−H modes. Nevertheless, the signal levels become small for transition moments characteristic of C−H motions.

In order to ensure adequate signal levels, dotriacontane was chosen for a sample because of its large methylene and low methyl concentrations.[45] In addition, the alkane concentrations were high in order to acquire adequate signals, especially for experiments involving the cross-peaks between the CH stretching and bending modes. The bending mode transition strength is significantly smaller than the stretching modes, so higher concentrations were required to accommodate the signal loss. The higher concentrations did cause distortions in the spectra because of absorption of the excitation beams entering the sample and the output signal leaving the sample. These absorption effects have been treated previously by Carlson.[46] They are described theoretically by multiplying the output intensity by an M-factor defined as

$$M = e^{-\alpha l}\left|\frac{e^{-i(K'-k')l} - 1}{(K'-k')l + i(\alpha - \alpha_{123})/2}\right|^2 \tag{2}$$

where $K \equiv K' + iK''$ is the complex wave-vector; $K' \equiv ((\omega_1 n_1 - \omega_2 n_2 + \omega_3 n_3))/(c)$; $K'' \equiv -(1/2)(\alpha_1 + +\alpha_2 + \alpha_3) \equiv -\alpha_{123}/2$; α_i and n_i are the absorption coefficient and refractive index for the i^{th} excitation beam; k' and α are the wave vector and absorption coefficient for the output beam, and l is the path length. This function is maximized for absorbances near 1 for the ω_1 excitation and above 1 for the ω_2 excitation. This behavior guided experiments with weak absorption at the ω_1 frequency and high absorption at the ω_2 frequency such as those involving cross peaks between the CH stretching mode and the bending mode.

3.0. Experimental Section

A Ti:sapphire regenerative amplifier pumped two optical parametric amplifiers (OPAs) at 790 nm to create tunable signal and idler frequencies. $AgGaS_2$ crystals created the two excitation frequencies by difference frequency mixing of the signal and idler frequencies. The output pulses were ~850 fs wide (fwhm), ~1−2 μJ energy, ~25 cm^{-1} bandwidth (fwhm) in the C−H stretch region and ~15 cm^{-1} in the C−H bend region. A beam splitter created the ω_2 and $\omega_{2'}$ beams from one OPA while the other OPA provided the ω_1 beam. Delay lines controlled the relative temporal positions of the three pulses. An off-axis parabolic mirror focused the three beams into the sample using a box phase-matching geometry at angles appropriate for the phase-matching condition $\vec{k}_4 = \vec{k}_1 - \vec{k}_2 + \vec{k}_{2'}$ The beam polarizations are identical. A second off-axis parabolic mirror directed the output to a monochromator and a mercury cadmium telluride detector measured the signal. A 5 μm long-pass filter was placed before the monochromator for experiments with ω_2 ~1450 cm^{-1} and ω_{m} ~ 2900 cm^{-1} in order to eliminate the scattered ω_2 light from the grating's second order.

Five variables control the TRIVE FWM experiment: the ω_1, ω_2 excitation frequencies, the ω_m monochromator frequency, and the $\tau_{21} \equiv \tau_2 - \tau_1$ and $\tau_{2'1} \equiv \tau_{2'} - \tau_1$ delay times where τ_i is the temporal position of pulse i. The delay times provide temporal discrimination, selection of specific coherence pathways, and measurements of the dephasing and population decay rate. For this work, ω_1 and ω_m are changed together so $\omega_m = \omega_1$, the output frequency expected for this phase-matching geometry. Typically, the multidimensional spectra have intensities that vary over orders of magnitude so the color bar scale is logarithmic.

Octane (C_8H_{18}) and dotriacontane ($C_{32}H_{66}$) were chosen as representative n-alkane samples because they have different methylene/methyl ratios. They were purchased from Aldrich and had 99% and 97% purities, respectively. The samples were diluted in carbon tetrachloride and placed in a 125 μm thick cell with 2 mm thick CaF_2 windows. For studies involving only the C−H stretches, the octane and dotriacontane concentrations were 0.18 and 0.03 M, respectively, in order to make the absorbance of the strongest IR feature at 2927 cm^{-1} ~1.1. For studies involving the C−H stretch and bend cross-peaks, the signals were smaller, so a saturated solution of dotriacontane in carbon tetrachloride was prepared. An excess of dotriacontane was added, the solution was equilibrated, decanted, then slightly diluted to prevent precipitation. If the solution is shaken or sonicated, a supersaturated solution readily forms. A 0.45 M solution was used for the same studies in octane.

4.0. Results

Figure 3 shows the FTIR spectra of the octane and dotriacontane solutions used for the C−H stretch studies and Table 1 summarizes the assignments, frequencies, and notation for the states of interest. While the methylene absorbances are of similar strength, the methyl modes are weak in the dotriacontane sample. Though the molar extinction coefficient increases for all C−H stretch modes as the carbon chain increases in length,[45] the relative number of methylene to methyl modes is much larger in dotriacontane. The methyl symmetric and asymmetric stretch modes (labeled CH_3-*ss* and CH_3-*as*, respectively) are located at 2870 cm^{-1} and 2956 cm^{-1}. The methylene symmetric stretch mode (labeled CH_2-*ss*) is located at 2854 cm^{-1}. The assignment of the 2927 cm^{-1} peak and the location of the methylene asymmetric mode is still uncertain. The 2927 cm^{-1} feature was first assigned as the methylene asymmetric mode, though bending overtone and combination bands were known to lie in this region. Oss first modeled the FTIR spectrum by including Fermi resonances between the CH_2-*ss* mode and methylene bending modes.[47] He later modeled the FTIR data by ignoring Fermi resonances and using just methylene asymmetric stretching modes.[48] More recent sum frequency generation (SFG) work on alcohols shows that the 2927 cm^{-1} feature involves a mixture of the methylene asymmetric stretch modes and Fermi resonances. Polarized SFG assigns a weak peak at 2926 cm^{-1} to the asymmetric stretch mode and two peaks at 2916 and 2954 cm^{-1} to Fermi resonances of the CH_2-*ss* mode with bending overtones and combination bands.[49] While these polarization studies appear to be unambiguous, Donaldson et al. recently used DOVE FWM to directly measure the bending

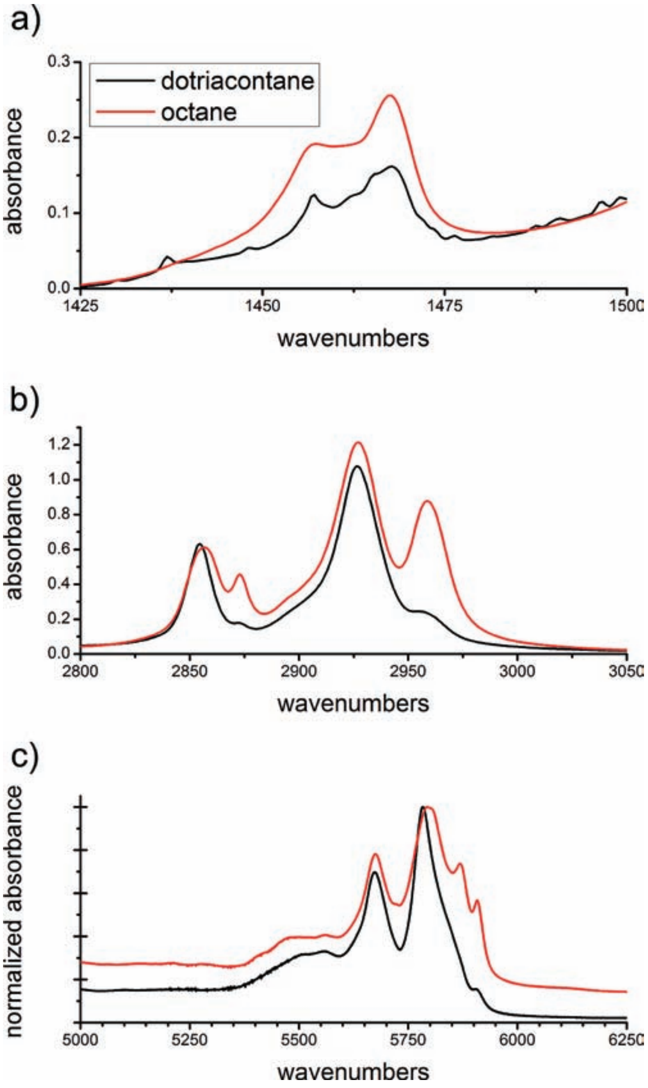

Figure 3. Infrared absorption spectra of the C−H (a) bending, (b) stretching, and (c) stretching overtone/combination band regions.

combination or overtone modes.[13] While they observed modes at 2927 cm^{-1}, they did not see a single strong mode. Instead, they saw signal throughout the C−H stretching region, with stronger peaks localized around 2900 cm^{-1} and 2950−2960 cm^{-1} that involved Fermi resonances.[13] Since there is certainly coupling of the modes at 2927 cm^{-1}, we reference this 2927 cm^{-1} feature as the methylene asymmetric stretch/Fermi resonance peak (labeled CH_2-*as/FR*). The bending modes at 1457 cm^{-1} and 1467 cm^{-1} are a methyl bend and a methylene scissors mode (labeled CH_3-*b* and CH_2-*b*, respectively). The DOVE-FWM spectrum shows a well-defined, narrow peak at ∼1468 cm^{-1} that is attributed to the methylene scissors mode.[13]

4.1. 2D Frequency/Frequency Spectra of Dotriacontane. Figure 4 shows the TRIVE spectra of the C−H stretching region of dotriacontane taken at different time delays. In Figure 4a, all three excitation pulses temporally overlap, and all of the coherence pathways in Figure 1 and Figure 2 are important. The diagonal features at $\omega_1 = \omega_2$ correspond to the CH_3-*as* (2956 cm^{-1}), the CH_2-*as/FR* modes (2927 cm^{-1}), the CH_3-*ss* (2870 cm^{-1}), and the CH_2-*ss* modes (2854 cm^{-1}). These positions match those seen in the FTIR spectrum. The CH_3-*ss* and CH_3-*as* modes are much weaker than the CH_2 modes. The CH_3-*ss* mode is only evident from the elongation along the diagonal of the CH_2-*ss* peak. There are also cross-peaks between the CH_2-*ss* and the CH_2-*as/FR* modes at $(\omega_1, \omega_2) = (2855, 2920)$ cm^{-1} and (2940, 2855) cm^{-1}. Note that the cross-peak positions are not symmetrical about the diagonal. The lower right cross-peak appears at the blue edge of the CH_2-*as/FR* peak ($\omega_1 = 2942$ cm^{-1}) whereas the upper left cross-peak appears at red side ($\omega_2 = 2920$ cm^{-1}). However, both cross-peaks are centered on the CH_2-*ss* mode.

Figure 4b−d shows the spectral changes that occur when pulses 2 and 2′ temporally overlap and pulse 1 occurs later. This time ordering corresponds to six pathways in Figure 1 and four pathways in Figure 2. These pathways are identical to pump−probe pathways. As the $\tau_{21} = \tau_{2'1}$ time delays increase, the methylene stretch cross-peak and diagonal features at $(\omega_1/\omega_m, \omega_2) = (2854, 2927)$ and (2854, 2854) cm^{-1} grow more intense while the diagonal CH_3-*as* feature at $\omega_1 = \omega_2 = \omega_m = 2870$ cm^{-1} becomes weak. Note also that the peaks appearing at $\omega_2 = 2854$ and 2927 cm^{-1} become much stronger at increasing delay times. Cross-peaks also appear between the methylene modes and the two methyl stretch modes. Additionally, the lower right cross-peak between the two methylene modes has shifted and now appears at the expected position where $(\omega_1/\omega_m, \omega_2) = (2854, 2927)$ cm^{-1}.

There are also weak features at lower ω_1 frequencies associated with overtones and combination bands. Figure 5a is a scale expansion of Figure 4 that shows features at $(\omega_1, \omega_2) = (2790, 2854)$ and (2770, 2920) cm^{-1}. The ω_2 values of these features match the frequencies of the CH_2-*ss* and CH_2-*as/FR* band transitions while the ω_1 frequencies are shifted because of the overtone and combination band anharmonicity.

4.2. 2D Frequency/Frequency Spectra of Octane. Figure 6 shows a similar series of TRIVE spectra in the C−H stretching region of octane with different time delays. In Figure 6a, the three excitation pulses temporally overlap, and all pathways again contribute to the spectra. The spectra are qualitatively similar to those of dotriacontane scans but have much stronger contributions from the methyl modes. The CH_3-*ss* peak at 2874 cm^{-1} is well-resolved now. The cross-peaks between the CH_2-*ss* peak and the CH_2-*as/FR* peak are also qualitatively similar except the upper left cross-peak has a doublet structure which was not observed in the dotriacontane spectrum. The two cross-peaks are still not symmetrically oriented relative to the diagonal. The lower right cross-peak appears at higher energy ($\omega_1 = 2935$ cm^{-1}) than the CH_2-*as/FR* peak while the upper left cross-peak is centered on the peak ($\omega_2 = 2925$ cm^{-1}). There is also a well-defined cross-peak at $(\omega_1, \omega_2) = (2874, 2920)$ cm^{-1} between the CH_3-*ss* peak and the CH_2-*as/FR* peak. A tail appears on the side of the CH_3-*as* diagonal-peak where $\omega_1 = 2970$ cm^{-1}. It is probably caused by unresolved cross-peaks between the CH_3-*as* modes and the CH_2-*as/FR* and the CH_3-*ss* mode.

Figure 6b−d shows the changes in the 2D spectrum as the ω_1 excitation is increasingly delayed from the ω_2 and $\omega_{2'}$ excitations. As in the dotriacontane spectra, new cross-peaks appear, and the same peaks involving the CH_2-*ss* become stronger while the diagonal CH_3-*ss* and CH_3-*as* modes grow weaker. Unlike dotriacontane, the CH_2-*ss* mode and its cross-peaks form doublet features. Additionally, the CH_3-*as* diagonal-peak and its cross-peaks form doublets as well. At the longest delay time, there are cross-peaks between all of the modes with the exception of those requiring an initial population in the CH_3-*ss* mode. Even the diagonal-peak associated with the CH_3-*ss* mode has become negligible.

Figure 5b shows that octane also has weak features in the region of overtones and combination bands at $(\omega_1, \omega_2) = (2790, 2854)$ and (2770, 2920) cm^{-1} but a third feature appears at (2790, 2960) cm^{-1}. The ω_2 value of the latter feature matches

TABLE 1

	assignment	frequency (cm^{-1})	label
Octane			
	methylene symmetric stretch, d^+	2854	CH_2-ss
	methyl symmetric stretch, r^+	2870	CH_3-ss
	methylene asymmetric stretch/Fermi resonance, d^-/FR	2927	CH_2-as/FR
	methyl asymmetric stretch, r^-	2956	CH_3-as
	methylene bending, δ	1470	CH_2-b
	methyl bending	1455	CH_3-b
Dotriacontane			
	methylene symmetric stretch, d^+	2854	CH_2-ss
	methyl symmetric stretch, r^+	2870	CH_3-ss
	methylene asymmetric stretch/Fermi resonance, d^-/FR	2927	CH_2-as/FR
	methyl asymmetric stretch, r^-	2956	CH_3-as
	methylene bending, δ	1470	CH_2-b
	methyl bending	1455	CH_3-b

the frequency of the CH_3-*as* transition while the ω_1 frequency matches that of the (2790, 2854) cm^{-1} feature.

4.3. 2D Time Delay and Frequency/Time Delay Dependencies. Figure 7 is a 2D plot of the intensity dependence on $\omega_1 = \omega_m$ and $\tau_{21} = \tau_{2'1}$ for $\omega_2 = 2926$ cm^{-1}. The $\omega_1 = \omega_m$ axis therefore corresponds to a cross section of Figure 6 at $\omega_2 = 2926$ cm^{-1}. This scan shows the evolution of the CH_2-*as/FR* diagonal-peak, and the related cross-peaks as a function of the $\tau_{21} = \tau_{2'1}$ pulse delay. Negative delays correspond to the ω_1 excitation following the ω_2 and $\omega_{2'}$ excitations, so this direction probes the population transfer time. Positive delays correspond to the ω_1 excitation preceding the other excitations, so this direction probes the dephasing time of the first coherence. The maximum intensity for the diagonal-peak occurs at −0.5 ps. In addition, there are changes in the peak shape and position along the $\omega_1 = \omega_m$ axis as the line shape evolves with the population time.

The feature at 2925 cm^{-1} corresponds to the CH_2-*as/FR* diagonal-peak while the features at 2850, 2875, and 2965 cm^{-1} correspond to three cross-peaks. The cross-peak intensity maximum is delayed and has a longer lifetime than the diagonal-peak. The cross-peaks grow in at different rates, suggesting that there is no single mechanism responsible for the cross-peaks. The lower energy modes have the longest lifetime. Additionally,

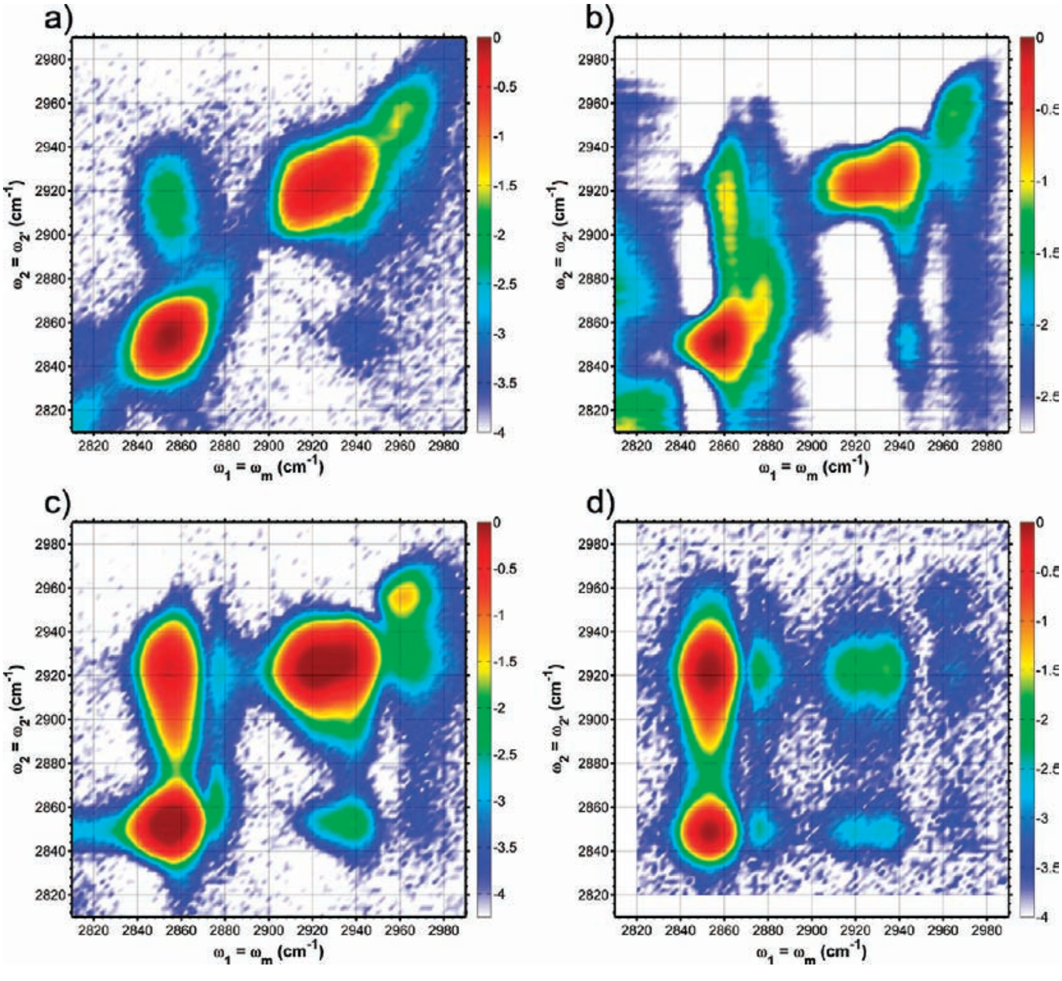

Figure 4. TRIVE FWM spectra of dotriacontane as a function of ω_1 and ω_2. The color bar indicates the logarithm of the intensity. $\tau_{21} = \tau_{2'1} =$ (a) 0 ps; (b) −0.5 ps; (c) −0.7 ps; (d) −6.0 ps.

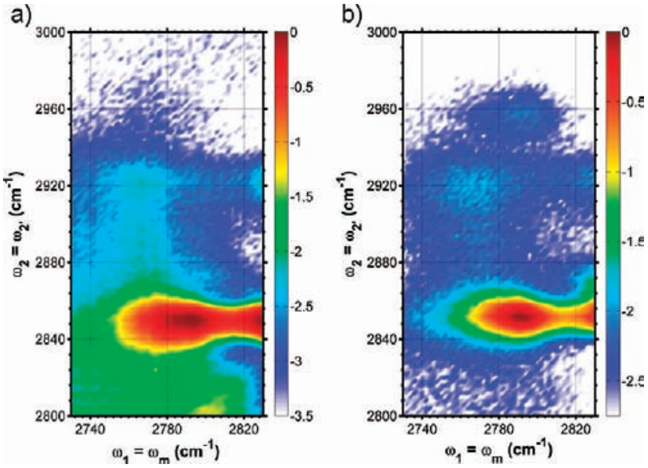

Figure 5. Expanded scale TRIVE FWM spectra of dotriacontane (a) and octane (b) as a function of ω_1 and ω_2 for −0.8 ps.

the line shapes and line positions evolve as the delay time increases. The CH_3-*as* peak clearly develops a new component near 2950 cm^{-1} as the peak splits. The CH_2-*ss* mode also develops a new component near 2840 cm^{-1} that is clearly seen at $\tau_{21} = -1$ ps, but it then decays at longer delay times.

Scanning the τ_{21} and $\tau_{2'1}$ delay times for fixed excitation and monochromator frequencies provides the complete temporal dependence of individual spectral features. Figure 8a,b contains delay scans in dotriacontane and octane, respectively, for the cross-peak between the CH_2-*ss* and the CH_2-*as/FR* modes at ($\omega_1 = \omega_m$, ω_2) = (2850, 2920) cm^{-1}. The delay times create the time orderings for all of the pathways shown in Figure 2. The arrows in the figure define the directions for the dephasing of each coherence or the relaxation of each population involved in the pathways. For example, the horizontal *v'v* arrow defines the direction of the *v'v* zero quantum coherence dephasing. The figure shows that the dephasing times of all the coherences created by the pathways in Figure 2 are faster than the excitation pulse durations, but the population transfer times are considerably longer. The population transfer is nonexponential with a decay time of ~3 ps.

Figure 9 shows the dependence of the weak features in Figure 5 on the $\tau_{21} = \tau_{2'1}$ delay times. The intensity increases rapidly for negative $\tau_{21} = \tau_{2'1}$ delay times and reaches a maximum at −0.8 ps. The decay is also very rapid and, except for the octane (2770, 2920) and (2790, 2960) cm^{-1} features, it is limited by the excitation pulse width. The latter two features have slightly longer decay times.

4.4. Cross-Peaks between Stretching and Bending Modes. Since frequency domain CMDS requires only short-term coherence between the excitation pulses, it is possible to use very different frequencies for ω_1 and ω_2. Figure 10 and Figure 11 show the 2D spectra for cross-peaks between the C−H stretching and the bending regions for dotriacontane and octane, respectively. The excitation pulses are temporally overlapped in Figure 10a and Figure 11a. Here, ω_2 and $\omega_{2'}$ are tuned to the stretching region, while ω_1 and ω_m are tuned to the bending region.

Figure 10a shows the C−H stretch/bending cross-peak region for dotriacontane with overlapped excitation pulses. The peaks near $\omega_1 = \omega_m = 1470$ cm^{-1} correspond to the methylene scissors mode, and the peaks near $\omega_1 = \omega_m = 1457$ cm^{-1} correspond to a methyl bend mode.[45] The methylene bending mode cross-peaks dominate the spectra, but there is a weaker contribution from the methyl bend mode. The peak near ($\omega_1 = \omega_m$, ω_2) = (1470, 2855) cm^{-1} is a CH_2-*b* and CH_2-*ss* cross-peak. There is little evidence of a cross-peak from the CH_2-*b* and CH_3-*ss* that would appear at ($\omega_1 = \omega_m$, ω_2) = (1470, 2870) cm^{-1}. The second cross-peak appears at ($\omega_1 = \omega_m$, ω_2) = (1470, 2920) cm^{-1} corresponding to the CH_2-*b* and CH_2-*as/FR* peak. Note that this peak is shifted from that seen in Figure 3 at 2927 cm^{-1}. It is also slightly shifted to the red from the position of the diagonal-peak observed in the stretching region scans. Figure 10b shows the same spectrum but with $\tau_{21} = \tau_{2'1} = -1.6$ ps. The spectrum is similar except for the appearance of a cross-peak between the CH_3-*b* and the CH_2-*ss* modes. The appearance of this new peak suggests it arises from population transfer from the initially excited CH_2-*ss*.

Figure 11a shows the 2D spectrum for octane when the three excitation pulses are temporally overlapped. The spectrum is similar to dotriacontane, but there is a greater contribution from the methyl modes. There are three peaks aligned with the CH_2-*b* mode at (ω_1, ω_2) = (1470, 2854), (1470, 2918), and (1470, 2954) cm^{-1}. Unlike dotriacontane, the cross-peak with the CH_2-*ss* is stronger than the CH_2-*as/FR* cross-peak. Aligned with the CH_3-*b* mode, there is a well-defined peak at (ω_1, ω_2) = (1455, 2954) cm^{-1} corresponding to coupling between the CH_3-*as* and the CH_3-*b* modes. This peak extends into the region around ω_2 = 2920 cm^{-1} involving the CH_2-*as/FR*. It also extends weakly into the region near the CH_3-*ss* mode at $\omega_2 = 2865$ cm^{-1}. Figure 11b shows the same spectrum with $\tau_{21} = \tau_{2'1} = -2$ ps. The CH_3-*b* cross-peaks show the greatest change. The CH_3-*as*/CH_3-*b* cross-peak has nearly vanished and left a broad and nearly featureless peak ranging from the CH_3-*as* mode to the CH_2-*as/FR* mode. In addition, the cross-peak between the CH_2-*as/FR* mode and the CH_3-*b* mode has greatly increased in relative amplitude.

5.0. Discussion

5.1. CH Stretching Region. Although dotriacontane and octane have different chain lengths and methyl/methylene ratios, their CMDVS spectra are still quite similar. More detailed observations require understanding the population and coherence dynamics. The discussion focuses on octane where the features and changes are better resolved but the same ideas apply to dotriacontane. Mixed frequency/time domain CMDVS is best performed with excitation pulses that are temporally similar to the coherence dephasing times in an experiment. Matching the excitation pulse width with the dephasing time optimizes both the spectral and the temporal resolution. Figure 8 shows the dephasing and population dynamics in this system. The rapid intensity decay in the directions of the *vg* and *v'g* arrows show that the dephasing times of coherences involving the methylene stretching modes are shorter than can be resolved by our excitation pulses. The slow decay in the direction of the *gg-vv* arrows shows that the population lifetime associated with the (ω_1, ω_2) = (2855, 2920) cm^{-1} cross-peak is much longer. The short dephasing times do not allow the use of the fully coherent TRIVE pathways[1] that can avoid the effects of population transfer on the spectra. Consequently, the spectra shown in this paper rely on pathways involving intermediate populations for which population transfer effects become important. There are many consequences in the spectra.

Figure 7 provides more insights into the dynamics of this system. The intensity of the diagonal feature at $\omega_1 = 2925$ cm^{-1} decays very quickly for positive $\tau_{21} = \tau_{2'1}$ so the *vg* single quantum coherence of the CH_2-*as/FR* peak must dephase rapidly after initial excitation by ω_1. The intensity decay is slower for negative delays where population relaxation determines the lifetime. The population lifetime is ~1 ps. The population lifetime depends upon the rates of ground state repopulation

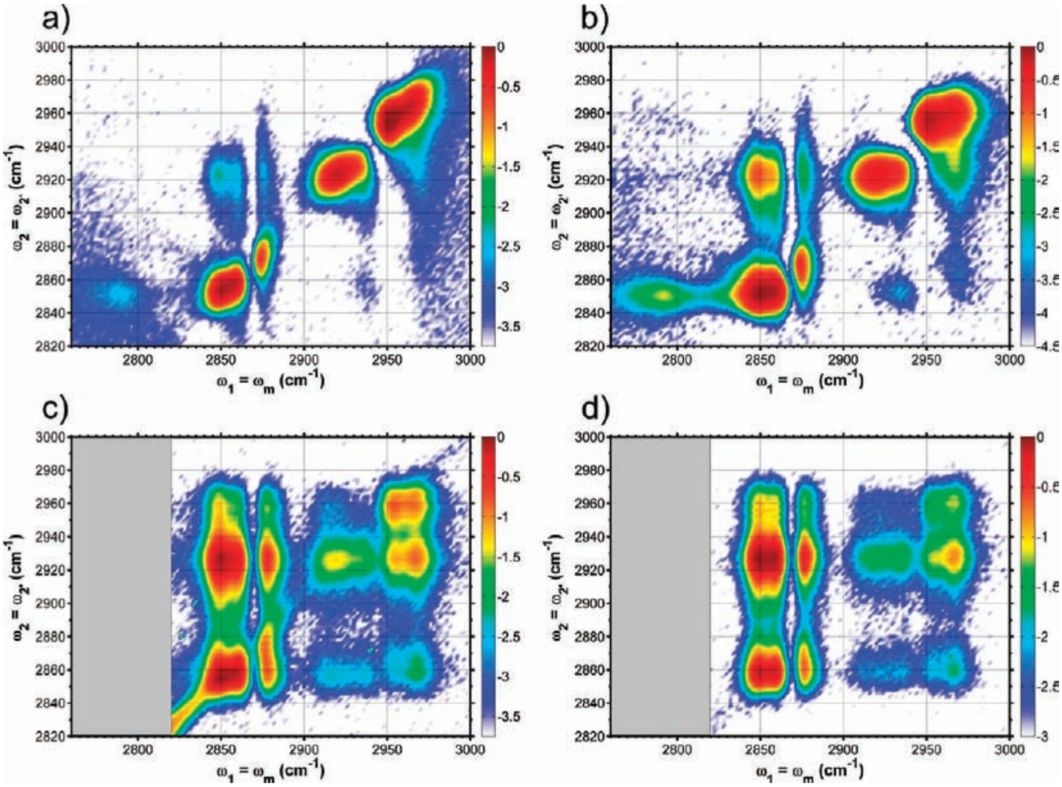

Figure 6. TRIVE FWM spectra of octane as a function of ω_1 and ω_2. The color bar indicates the logarithm of the intensity. $\tau_{21} = \tau_{2'1} =$ (a) 0 ps; (b) -0.8 ps; (c) -4.0 ps; (d) -6.0 ps. Spectra were not acquired in the gray areas.

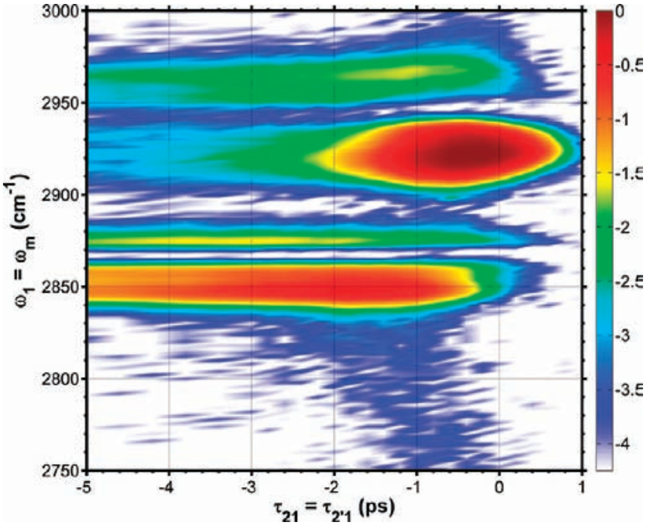

Figure 7. Mixed frequency/time domain plot of TRIVE FWM in octane with $\omega_2 = 2926$ cm^{-1} and $\omega_1 = \omega_m$ $\tau_{21} = \tau_{2'1}$scanned against $\tau_{21} = \tau_{2'1}$. The color bar indicates the logarithm of the intensity. The feature at $\omega_1 = \omega_m = 2926$ cm^{-1} is a diagonal-peak in Figure 5 while the others are cross-peaks.

and the vibrational state decay, Γ_{gg} and $\Gamma_{v'v'}$. Note that this decay is significantly faster than the ~2.5 ps decay time of the (ω_1, ω_2) = (2855, 2920) cm^{-1} cross-peak in Figure 8. In addition, the peak of the intensity is delayed by ~2 ps indicating that population transfer from the CH$_2$-*as/FR* population is important. Both features have contributions from the CH$_2$-*as*/FR population so the cross-peak must have additional contributions to its intensity. We attribute the longer decay time to population transfer to lower energy states that have longer lifetimes and are coupled to the CH$_2$-*ss* mode. For example, $gg \xrightarrow{-2} gv' \xrightarrow{2'} v'v' \Rightarrow xx \xrightarrow{1} x + v,x$ is a representative pathway. The figure also shows that the spectral features associated with the other modes are enhanced as well by the decay of the CH$_2$-*as/FR* population decay but the growth and decay rates differ. We interpret these dynamics also in terms of the two mechanisms for population transfer enhancement of cross-peaks. The growth of the intensity of the CH$_2$-*ss* mode is the result of direct population transfer from the CH$_2$-*as/FR* mode. The two methyl modes also appear as a result of the CH$_2$-*as/FR* mode population transfer but their rates differ. The CH$_3$-*as* cross-peak appears more quickly and then decays more rapidly than the CH$_3$-*ss* mode. Its central frequency also shifts. These changes are signatures of population transfer to states that are coupled to the methyl modes. Population transfer is probably occurring to the CH$_2$-*ss* mode and to lower energy modes that are coupled to the methyl stretch modes. The changes in the central frequency depend on the anharmonicity of the CH$_3$-*as* transitions from the CH$_2$-*ss* and lower energy states.

The 2D spectra in Figure 4 and Figure 6 reflect the rapid dephasing rates and population transfer. Since the coherence dephasing rates are fast compared with the excitation pulse widths, the spectra are dominated by the pathways in Figure 1 and Figure 2 that involve intermediate populations. For the cross-peaks, these pathways depend upon ω_2 and $\omega_{2'}$ interacting before ω_1. When all three pulses are temporally overlapped, the cross-peaks are weak and are not symmetrically located. The lower right cross-peak is significantly blue-shifted relative to the center of the CH$_2$-*as/FR* peak whereas the upper left cross-peak appears at the center frequency of the CH$_2$-*as/FR* peak. The lower right cross-peak at (ω_1, ω_2) = (2925, 2854) cm^{-1} corresponds to ω_2 and $\omega_{2'}$ exciting the CH$_2$-*ss* mode followed by ω_1 exciting the CH$_2$-*as* or Fermi resonance state within the band at 2927 cm^{-1}. We believe that this cross-peak results from anharmonic coupling with the Fermi resonance state. There

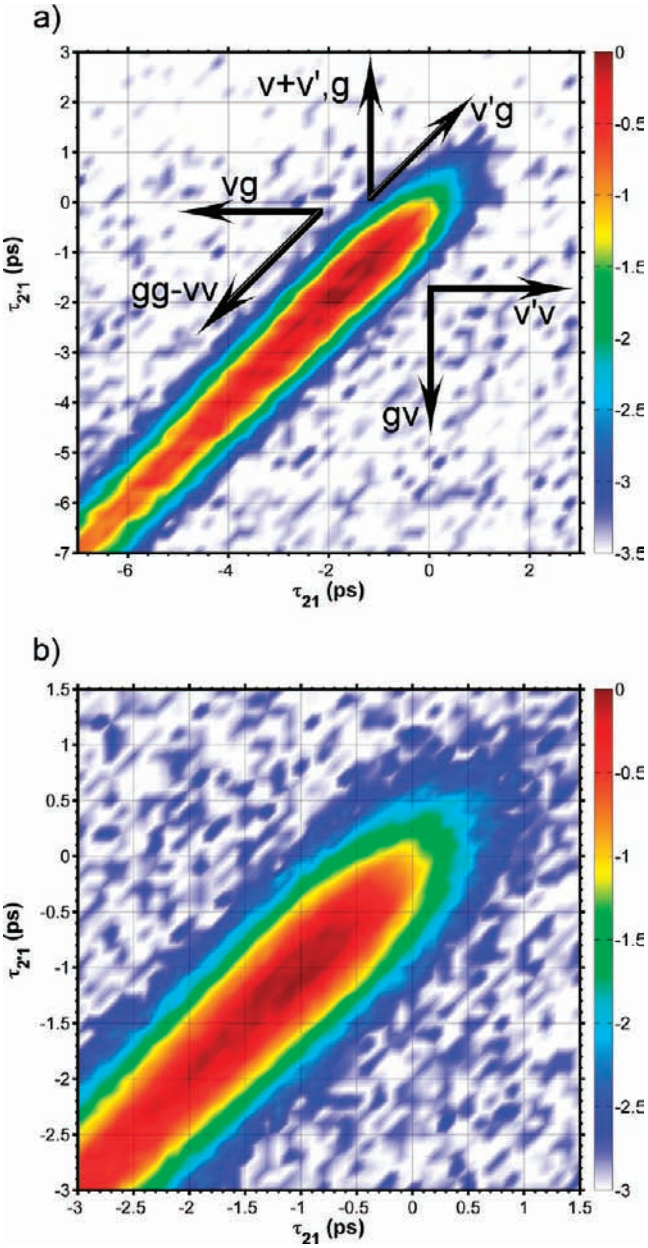

Figure 8. Two dimensional scans of the time delays for the (a) upper left dotriacontane and (b) octane cross-peaks at (ω_1, ω_2, ω_m) = (2852, 2920, 2852) and (2850, 2920, 2850) cm^{-1}, respectively. The arrows in (a) indicate the direction in which dephasing or population decay occurs for the coherences or populations indicated by the letters. The color bar indicates the logarithm of the intensity.

should then be a cross-peak at (ω_1, ω_2) = (2854, 2925) cm^{-1} corresponding to ω_2 and $\omega_{2'}$ exciting the Fermi resonance state followed by ω_1 exciting the CH$_2$-*ss*. There is no indication of a peak at this position. Its absence is attributed to a very short population lifetime of the Fermi resonance peak. In addition, the diagonal feature at 2925 cm^{-1} is asymmetric and has a tail at ω_1 = 2934 cm^{-1} for octane and 2943 cm^{-1} for dotriacontane, the same frequency as the lower right cross-peak. It is particularly prominent for octane. The shape and the tail are suggestive that this unresolved state couples with states near 2900−2910 cm^{-1} in the absorption spectrum as well as the CH$_2$-*ss* mode cross-peak at (ω_1, ω_2) = (2934, 2855) cm^{-1}.

Although the upper left cross-peak at (ω_1, ω_2) = (2855, 2925) cm^{-1} is somewhat weak, it becomes considerably stronger as the $\tau_{21} = \tau_{2'1}$ delay time increases. The ω_2 value is centered at the middle of the CH$_2$-*as/FR* feature. We attribute this cross-peak to rapid population transfer of the CH$_2$-*as/FR* to the CH$_2$-*ss* mode or lower states followed by ω_1 creating an output

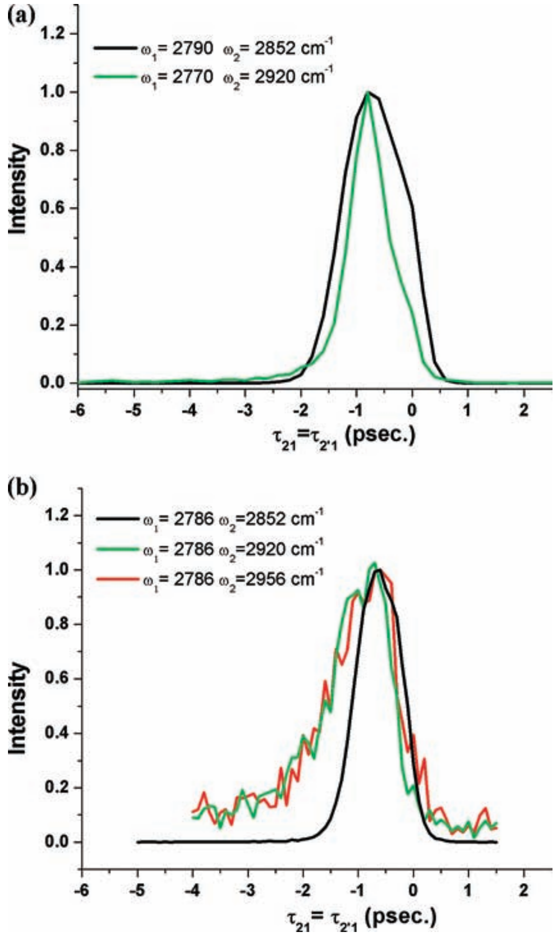

Figure 9. Dependence of the dotriacontane (a) and octane (b) TRIVE FWM signal on the time delays for the features at (ω_1, ω_2) = (2790, 2854), (2770, 2920), and (2790, 2960) cm^{-1}.

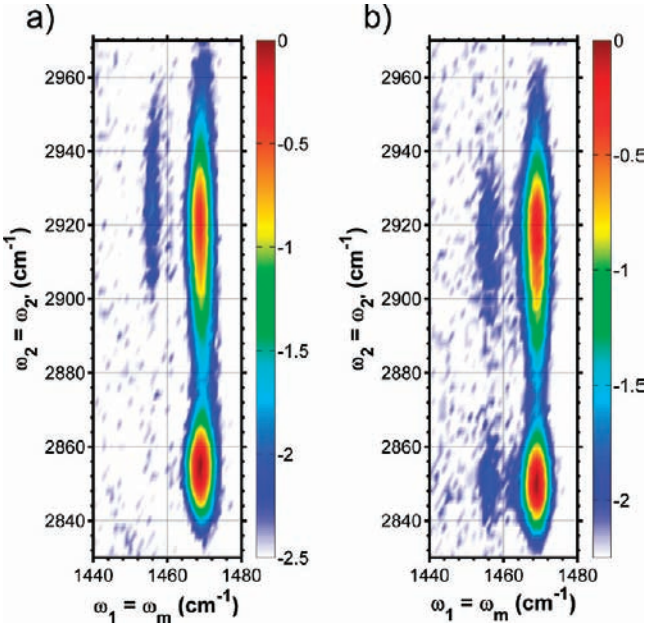

Figure 10. TRIVE FWM spectra of dotriacontane in the cross-peak region involving the C−H defomation and stretching modes as a function of ω_1 and ω_2. The color bar indicates the logarithm of the intensity. (a) 0 ps; (b) −1.56 ps.

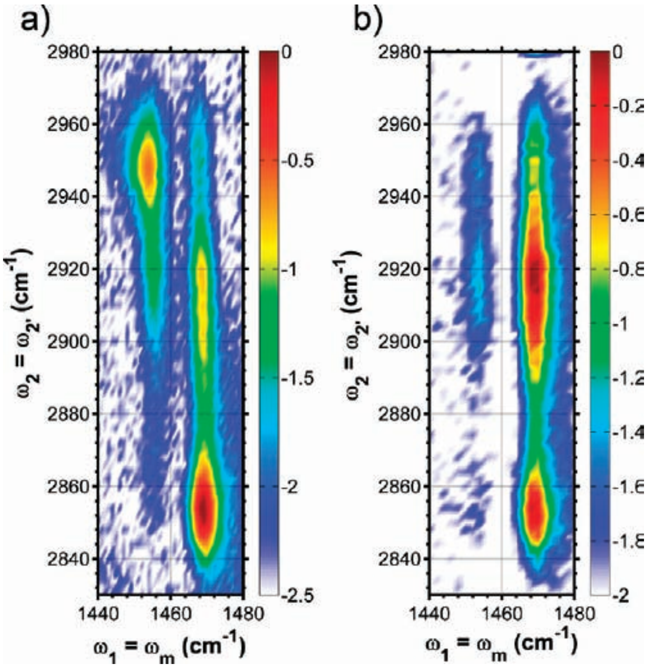

Figure 11. TRIVE FWM spectra of octane in the cross-peak region involving the C−H defomation and stretching modes as a function of ω_1 and ω_2. The color bar indicates the logarithm of the intensity. (a) 0 ps; (b) −2.0 ps.

coherence involving the CH_2-*ss* mode, $gg \xrightarrow{-2} gv' \xrightarrow{2'} v'v' \Rightarrow xx \xrightarrow{1} vg$ where xx can be vv. We do not attribute it to anharmonic coupling between symmetric and asymmetric modes because the companion cross-peak in the lower right would be equally important. However, that cross-peak is shifted to higher frequency and is attributed to coupling with an unresolved state in the 2925 cm^{-1} band. In addition, the rapid decay of the CH_2-*ss* feature at $\omega_1 = 2850$ cm^{-1} in Figure 7 at positive delay times indicates that pathways like $gg \xrightarrow{1} v'g \xrightarrow{-2} v'v \xrightarrow{2'} v'g$ do not contribute appreciably because of the low amount of anharmonic coupling between the two states.

The CH_3-*as* mode has similar characteristics. At short delay times, it also has a tail on the blue edge of the diagonal feature that extends into the region of the CH_3-*ss* mode. At later delay times, a clear cross-peak develops at $(\omega_1, \omega_2) = (2970, 2870)$ cm^{-1} in the lower right of Figure 6 between the two methyl modes, but as the delay time increases, its frequency shifts to $(\omega_1, \omega_2) = (2967, 2855)$ cm^{-1}. The shift is accompanied by a corresponding shift in the position and intensity of the diagonal CH_3-*ss* feature. Initially, the diagonal CH_3-*ss* feature appears at the expected position, but it broadens and disappears as a new cross-peak appears at longer delay times. These observations suggest that the 2D spectra are resolving different states lying within the absorption band at 2955 cm^{-1} that couple differently with the CH_3-*ss* mode. The cross-peak that appears for temporally overlapped excitation pulses may reflect anharmonic coupling between the CH_3-*ss* and a state within the CH_2-*as/FR* mode absorption band. However, the shifts and intensity changes with increasing $\tau_{21} = \tau_{2'1}$ suggest that population transfer must also be important. The population transfer can involve relaxation from the initially excited CH_3-*as* mode to the CH_3-*ss* and to lower modes. We also note that population transfer from the methyl stretching modes is not as effective in creating cross-peaks with the methylene modes. In fact, no cross-peaks are observed at long delay times when the CH_3-*ss* mode is excited. This observation suggests that the methyl stretch modes relax to states that are less coupled to the methylene stretch modes and consequently are less able to create cross-peaks with the methylene modes.

Many of the spectral features in Figure 4 and Figure 6 became doublets along the $\omega_1 = \omega_m$ axis at long delay times. On the other hand, the ω_2 frequencies of each spectral feature in Figures 4, 6, and 7 match the peak positions expected from the infrared spectrum. The relative intensities also follow the absorption strengths of each transition. This correspondence arises because the ω_2 frequency determines the population excitation efficiency. Population transfer then occurs and the excited population is divided between different states of the system. The ω_1 excitation then excites a methyl or methylene stretch mode from each populated state. Features are observed at both the expected frequencies and new frequencies that reflect the anharmonic coupling associated with each ω_1 transition from the different populated states. Many of the features appear as doublets with one peak appearing at the expected position and a second appearing at a shifted position because of the new anharmonic coupling associated with recently populated state(s). The relative intensities for different values of ω_1 depend on the relative absorption strengths of the different transitions and the coupling of the different populated states to the different transitions.

Overtone and combination band transitions in Figure 5 are expected to arise from pathways involving $(2v,v)$ and $(v + v',v)$ output coherences and intermediate vv populations and $v'v$ zero quantum coherences. The spectra of dotriacontane (Figure 5a) and octane (Figure 5b) are similar except for the absence of the feature at $(\omega_1, \omega_2) = (2790, 2960)$ cm^{-1} in the dotriacontane spectrum. The absence is expected because the methyl feature is much weaker in dotriacontane. The features in these spectra also have a similar dependence on the $\tau_{21} = \tau_{2'1}$ time delays. The discussion will therefore focus on the octane spectrum.

The strongest peak at $(\omega_1, \omega_2) = (2790, 2854)$ cm^{-1} is assigned to the CH_2-*ss* overtone since it is near the expected location of the overtone. For alkanes, the methyl and methylene overtones are expected to be red-shifted approximately 60 cm^{-1} from the diagonal-peaks.[50−52] The time dependence in Figure 9 indicates this feature depends only on pathways with intermediate populations that dominate at negative $\tau_{21} = \tau_{2'1}$ delay times. These pathways create an excited CH_2-*ss* mode population which undergoes rapid decay compared with the excitation pulse width. The decay is also much faster than the relaxation of the CH_3-*ss* diagonal-peak at (2854, 2854) cm^{-1}. The overtone peak depends on Γ_{vv} while the diagonal-peak depends on both Γ_{vv} and Γ_{gg}. The rapid decay of the overtone peak and the longer decay of the diagonal-peak indicates that Γ_{gg} is much slower than Γ_{vv}.

The weaker peaks at $(\omega_1, \omega_2) = (2770, 2920)$ and (2790, 2960) cm^{-1} correspond to ω_2 values that excite populations in the CH_2-*as/FR* and CH_3-*as* modes, respectively. The ω_1 frequencies of these features are near the CH_2-*ss* overtone frequency. We assign these features to population transfer pathways such as $gg \rightarrow gv' \rightarrow v'v' \Rightarrow vv \rightarrow 2v,v$. The (2790, 2960) cm^{-1} feature has the same ω_1 frequency as the (2790, 2854) cm^{-1} feature as would be expected if the 2790 cm^{-1} state is the CH_2-*ss* overtone. However, the (2770, 2820) cm^{-1} feature is significantly shifted. We attribute the shift to the excitation of a low energy vibrational mode through the excess energy resulting from the population transfer, $gg \rightarrow gv' \rightarrow v'v' \Rightarrow x + v,x + v \rightarrow x + 2v,x + v$. The presence of this low energy mode must create the additional anharmonic shift. The shift is not observed when the CH_3-*as* mode relaxes to the CH_2-*ss* mode because different low-lying vibrational or bath states are excited. This assignment is consistent with our interpretation that the cross-peaks result from population transfer rather than direct anharmonic coupling between two modes. If direct anharmonic coupling were important, combination bands would appear because of pathways like

$$gg \rightarrow gv \rightarrow v'v \rightarrow v + v', v$$

These two features also have a longer decay time in octane than the (2790, 2854) cm^{-1} feature. Since the CH$_2$-*ss* mode must have a short lifetime, the longer decay time must result from longer lifetimes for the states that feed the CH$_2$-*ss* mode. These longer lifetimes are not observed in the dotriacontane features.

The assignment of the (2790, 2854) cm^{-1} feature to the CH$_2$-*ss* overtone predicts the presence of an overtone peak in the near-infrared region at 5644 cm^{-1}. Figure 3c shows the near-infrared spectrum in this region, and there is a strong peak at 5678 cm^{-1} but none at the expected location. The near-infrared spectrum is consistent with previous work that assigned this peak to the CH$_2$-*ss* overtone transition.[52]

We see no evidence for peaks in Figure 4 and Figure 6 arising from pathways involving the combination bands and other overtones. These peaks would be red-shifted along the abscissa by the anharmonicity if the third excitation pulse is ω_1 and red-shifted along the ordinate by the anharmonicity if the third excitation pulse is ω_2. The overtone peak intensity depends on the anharmonicity and the Γ_{vv}, Γ_{vg}, and $\Gamma_{2v,v}$ population transferand dephasing rates. A number of factors may contribute to their absence. First, the direct coupling between the C−H modes is weak, so population transfer is more important for creating cross-peaks than direct coupling. Second, overtone and combination band states have faster dephasing rates than fundamental modes, so they are broader and their coherences dephase more quickly. Both effects result in lower signal intensity. Third, the nonparametric pathways involving combination bands and overtones depend on the relaxation rate of an excited state population while the pathways involving only the fundamental modes also include the relaxation rate that repopulates the ground state. The ground state repopulation rate is appreciably slower than the excited state relaxation rate and consequently pathways involving the ground state population dominate. In addition, little is known about the nature of the CH$_2$-*as* mode, and it may have a particularly rapid relaxation. Finally, the expected location of the CH$_2$-*as* overtone peak is obscured by a cross-peak between the CH$_2$-*ss* and the CH$_2$-*as* located at (ω_1, ω_2) = (2854, 2920 cm^{-1}).

5.2. CH Bend-CH Stretching Region. The cross-peaks between the methyl and methylene stretching modes and the bending modes have similar interpretations. Our discussion focuses on octane, but dotriacontane has the same explanations. The CH$_2$-*b* mode shows strong cross-peaks with the CH$_2$-*ss* at (ω_1, ω_2) = (1470, 2854) cm^{-1} and CH$_2$-*as/FR* modes at (ω_1, ω_2) = (1470, 2915) cm^{-1}. The CH$_3$-*as* mode has a cross-peak with CH$_3$-*b* mode at (ω_1, ω_2) = (1455, 2948) cm^{-1}. Both appear because of anharmonic coupling between the two modes. Note that the ω_2 position for the CH$_2$-*as/FR* feature appears on the red side of the absorption line. This shift is another indication that the 2D spectrum is resolving states that lie within the infrared absorption band at 2927 cm^{-1}. Comparison of the cross-peaks in Figure 6 and Figure 11a at (ω_1, ω_2) = (2940, 2854) and (1470, 2915) cm^{-1}, respectively, suggests the peaks are resolving states at 2915 and 2940 cm^{-1} within the CH$_2$-*as/FR* band at 2927 cm^{-1}.

The spectral changes occurring at increased delay times reflect population transfer effects. The CH$_2$-*as/FR* peak grows brighter while the CH$_3$-*as* mode peak becomes fainter. Excitation of the CH$_2$-*as* results in direct population transfer to the CH$_2$-*b* mode from which ω_1 creates the output coherence. Population transfer that follows excitation of the CH$_3$-*as* results in states that do not couple to the CH$_3$-*b* mode, so the cross-peak is weak. On the other hand, excitation of the methylene modes does result in population transfer to states that couple to the methyl bend mode so weak cross-peaks appear in the spectra.

Donaldson et al. measured the DOVE FWM spectrum for hexane in this same region.[13] They observed cross-peaks between the methylene scissors mode at 1470 cm^{-1} and states at 2900 and 2950 cm^{-1}. DOVE-FWM selectively measures combination band transitions while TRIVE FWM measures anharmonically coupled transitions. We believe that the states at 2900 and 2950 cm^{-1} involve different states than the ones involved in our experiment.

6.0. Conclusions

This paper has examined the multidimensional TRIVE FWM spectra of methylene and methyl stretching and bending modes in two representative alkanes. The spectra are a sensitive function of the delay time and provide important insights to the nature of the vibrational relaxation and coherence dephasing processes of the C−H modes and the dynamics between them. The dephasing times of the methyl and methylene stretch modes are shorter than the excitation pulses in our experiments and prevent the use of fully coherent pathways. In addition, the anharmonic coupling is weak so the TRIVE FWM spectra contain only weak cross-peaks between vibrational modes that result from population transfer between the C−H stretching modes and transfer to other lower energy modes. Population transfer causes intensity changes and apparent peak position shifts in the spectra. The 2D spectra contain cross-peaks at frequencies that are shifted from those measured in infrared absorption spectra. Their spectral positions define the frequencies of states that are not resolved in infrared absorption spectra. The experiments also defined the dynamics of population transfer among the different C−H modes and to lower energy modes that are anharmonically coupled to the C−H stretching modes.

Acknowledgment. This work was supported by the National Science Foundation under Grant CHE-0650431.

References and Notes

(1) Pakoulev, A. V.; Rickard, M. A.; Meyers, K. A.; Kornau, K.; Mathew, N. A.; Thompson, D. C.; Wright, J. C. *J. Phys. Chem. A* **2006**, *110*, 3352.

(2) Jonas, D. M. *Annu. Rev. Phys. Chem.* **2003**, *54*, 425.

(3) Scheurer, C.; Mukamel, S. *J. Chem. Phys.* **2002**, *116*, 6803.

(4) Zhao, W.; Wright, J. C. *Phys. Rev. Lett.* **2000**, *84*, 1411.

(5) Mandal, P. K.; Majumdar, A. *Concepts in Magnetic Resonance Part A* **2004**, *20A*, 1.

(6) Wright, J. C. *Int. Rev. Phys. Chem.* **2002**, *21*, 185.

(7) LaBuda, M. J.; Wright, J. C. *Chem. Phys. Lett.* **1998**, *290*, 29.

(8) LaBuda, M. J.; Wright, J. C. *J. Chem. Phys.* **1998**, *108*, 4112.

(9) LaBuda, M. J.; Wright, J. C. *Phys. Rev. Lett.* **1997**, *79*, 2446.

(10) Hamilton, J. P.; LaBuda, M. J.; Wright, J. C. *Chem. Phys. Lett.* **1997**, *277*, 175.

(11) Fournier, F.; Gardner, E. M.; Kedra, D. A.; Donaldson, P. M.; Guo, R.; Butcher, S. A.; Gould, I. R.; Willison, K. R.; Klug, D. R. *Proc. Natl. Acad. Sci. U.S.A.* **2008**, *105*, 15352.

(12) Fournier, F.; Gardner, E. M.; Guo, R.; Donaldson, P. M.; Barter, L. M. C.; Palmer, D. J.; Barnett, C. J.; Willison, K. R.; Gould, I. R.; Klug, D. R. *Anal. Biochem.* **2008**, *374*, 358.

(13) Donaldson, P. M.; Guo, R.; Fournier, F.; Gardner, E. M.; Gould, I. R.; Klug, D. R. *Chem. Phys.* **2008**, *350*, 201.

(14) Donaldson, P. M.; Guo, R.; Fournier, F.; Gardner, E. M.; Barter, L. M. C.; Barnett, C. J.; Gould, I. R.; Klug, D. R.; Palmer, D. J.; Willison, K. R. *J. Chem. Phys.* **2007**, 127.

(15) Zhao, W.; Wright, J. C. *J. Am. Chem. Soc.* **1999**, *121*, 10994.

(16) Zhao, W.; Wright, J. C. *Phys. Rev. Lett.* **1999**, *83*, 1950.

(17) Meyer, K. A.; Thompson, D. E.; Wright, J. C. *J. Phys. Chem. A* **2004**, *108*, 11485.

(18) Besemann, D. M.; Meyer, K. A.; Wright, J. C. *J. Phys. Chem. B* **2004**, *108*, 10493.

(19) Meyer, K. A.; Besemann, D. M.; Wright, J. C. *Chem. Phys. Lett.* **2003**, *381*, 642.

(20) Naraharisetty, S. R. G.; Kasyanenko, V. M.; Rubtsov, I. V. *J. Chem. Phys.* **2008**, *128*, 104502.

(21) Kurochkin, D. V.; Naraharisetty, S. R. G.; Rubtsov, I. V. *Proc. Natl. Acad. Sci. U.S.A.* **2007**, *104*, 14209.

(22) Kurochkin, D. V.; Naraharisetty, S. R. G.; Rubtsov, I. V. *J. Phys. Chem. A* **2005**, *109*, 10799.

(23) Sibert, E. L.; Hutchinson, J. S.; Reinhardt, W. P.; Hynes, J. T. *Int. J. Quantum Chem.* **1982**, 375.

(24) Hutchinson, J. S.; Reinhardt, W. P.; Hynes, J. T. *J. Chem. Phys.* **1983**, *79*, 4247.

(25) Gelman, D.; Schwartz, S. D. *J. Chem. Phys.* **2009**, 130.

(26) Laubereau, A.; Kaiser, W. *Rev. Mod. Phys.* **1978**, *50*, 607.

(27) Monson, P. R.; Patumtev, S.; Kaufmann, K. J.; Robinson, G. W. *Chem. Phys. Lett.* **1974**, *28*, 312.

(28) Weston, R. E.; Flynn, G. W. *Annu. Rev. Phys. Chem.* **1992**, *43*, 559.

(29) Vandenbout, D.; Freitas, J. E.; Berg, M. *Chem. Phys. Lett.* **1994**, *229*, 87.

(30) McIlroy, A.; Nesbitt, D. J. *J. Chem. Phys.* **1994**, *101*, 3421.

(31) Tominaga, K.; Yoshihara, K. *Phys. Rev. Lett.* **1996**, *76*, 987.

(32) Lehmann, K. K.; Scoles, G.; Pate, B. H. *Annu. Rev. Phys. Chem.* **1994**, *45*, 241.

(33) Nesbitt, D. J.; Field, R. W. *J. Phys. Chem.* **1996**, *100*, 12735.

(34) Stewart, G. M.; Mcdonald, J. D. *J. Chem. Phys.* **1983**, *78*, 3907.

(35) Alfano, R. R.; Shapiro, S. L. *Phys. Rev. Lett.* **1972**, *29*, 1655.

(36) Sibert, E. L.; Ramesh, S. G.; Gulmen, T. S. *J. Phys. Chem. A* **2008**, *112*, 11291.

(37) Fendt, A.; Fischer, S. F.; Kaiser, W. *Chem. Phys.* **1981**, *57*, 55.

(38) Laenen, R.; Rauscher, C. *Chem. Phys. Lett.* **1997**, *274*, 63.

(39) Laenen, R.; Rauscher, C.; Laubereau, A. *Chem. Phys. Lett.* **1998**, *283*, 7.

(40) Iwaki, L. K.; Dlott, D. D. *Chem. Phys. Lett.* **2000**, *321*, 419.

(41) Iwaki, L. K.; Dlott, D. D. *J. Phys. Chem. A* **2000**, *104*, 9101.

(42) Wright, J. C. Nonlinear Spectroscopy and Coherent Multidimensional Spectroscopy. In *Lasers in Chemistry; 1 ed.*; Lackner, M., Ed.; Wiley-VCH Verlag: Weinheim, 2008; Vol. 1, pp 173.

(43) Wright, J. C.; Carlson, R. J.; Hurst, G. B.; Steehler, J. K.; Riebe, M. T.; Price, B. B.; Nguyen, D. C.; Lee, S. H. *Int. Rev. Phys. Chem.* **1991**, *10*, 349.

(44) Prior, Y.; Bogdan, A. R.; Dagenais, M.; Bloembergen, N. *Phys. Rev. Lett.* **1981**, *46*, 111.

(45) Jones, R. N. *Spectrochim. Acta* **1957**, *9*, 235.

(46) Carlson, R. J.; Wright, J. C. *Appl. Spectrosc.* **1989**, *43*, 1195.

(47) Marinkovic, T.; Oss, S. *Phys. Chem. Commun.* **2002**, *5*, 66.

(48) Marinkovic, T.; Oss, S. *Phys. Chem. Commun.* **2003**, *6*, 42.

(49) Lu, R.; Gan, W.; Wu, B. H.; Chen, H.; Wang, H. F. *J. Phys. Chem. B* **2004**, *108*, 7297.

(50) Greenlay, W. R. A.; Henry, B. R. *J. Chem. Phys.* **1978**, *69*, 82.

(51) Oss, S. *J. Mol. Struct.* **2006**, *87*, 780–781.

(52) Ricard-Lespade, L.; Longhi, G.; Abbate, S. *Chem. Phys.* **1990**, *142*, 245.

JP905172P